Simulating the radiation loss of superconducting submillimeter wave filters and transmission lines using Sonnet em

Endo, Akira; Pascual Laguna, Alejandro; Hähnle, Sebastian; Karatsu, Kenichi; Thoen, David J.; Murugesan, Vignesh; Baselmans, Jochem J.A.

DOI
10.1117/1.JATIS.8.3.036005

Publication date
2022

Document Version
Final published version

Published in
Journal of Astronomical Telescopes, Instruments, and Systems

Simulating the radiation loss of superconducting submillimeter wave filters and transmission lines using Sonnet *em*

Akira Endo[a,*] **Alejandro Pascual Laguna**[a,b] **Sebastian Hähnle**[a,b] **Kenichi Karatsu**[a,b] **David J. Thoen**[a] **Vignesh Murugesan**[b] **and Jochem J.A. Baselmans**[a,b]

[a]Delft University of Technology, Faculty of Electrical Engineering, Mathematics and Computer Science, Delft, The Netherlands
[b]SRON—Netherlands Institute for Space Research, Leiden, The Netherlands

Abstract. Superconducting resonators and transmission lines are fundamental building blocks of integrated circuits for millimeter-submillimeter (mm-submm) astronomy. Accurate simulation of radiation loss from the circuit is crucial for the design of these circuits because radiation loss increases with frequency, and can thereby deteriorate the system performance. Here, we show a stratification for a 2.5-dimensional method-of-moment simulator Sonnet *em* that enables accurate simulations of the radiative resonant behavior of submm-wave coplanar resonators and straight coplanar waveguides. The Sonnet simulation agrees well with the measurement of the transmission through a coplanar resonant filter at 374.6 GHz. Our Sonnet stratification utilizes artificial lossy layers below the lossless substrate to absorb the radiation, and we use co-calibrated internal ports for de-embedding. With this type of stratification, Sonnet can be used to model superconducting mm-submm wave circuits even when radiation loss is a potential concern. [DOI: 10.1117/1.JATIS.8.3.036005]

Keywords: millimeter-wave; astronomy; simulations; submillimeter-wave; kinetic inductance detectors; integrated superconducting spectrometer.

Paper 21130 received Oct. 12, 2021; accepted for publication Sep. 9, 2022; published online Sep. 28, 2022.

1 Introduction

Superconducting microwave resonators are used in astronomical instrumentation,[1–3] quantum computation,[4,5] and solid-state physics.[6] For designing the resonators and the superconducting transmission line circuit around it, the planar method of moment (MoM) simulation software Sonnet *em*[7] (Sonnet, hereafter) is widely used. This is because Sonnet requires less simulation time compared to full three-dimensional (3D) simulators (e.g., CST Microwave Studio[8] and HFSS[9]) for planar structures,[10] and it is straightforward to model superconductors in Sonnet.[11,12]

In recent years, there is an increasing demand in astronomical instrumentation for superconducting circuits that operate in the millimeter-submillimeter (mm-submm) band up to 1 THz.[1,13] At above ∼100 GHz, radiation losses become significant for coplanar structures, and the quality factor of resonators can deteriorate.[14] While full 3D simulators can simulate free-space boundaries, Sonnet requires a perfect electrical conductor (PEC) surface on the four walls perpendicular to the planar structures. This can lead to problems, such as suppression of radiative modes, reflections from the walls back to the circuit, and standing waves. Recently, we have reported that the radiation loss of a straight coplanar waveguide (CPW) can be accurately modeled with Sonnet using a box that is sufficiently large to allow all radiative modes to be excited, and a stratification that prevents reflection from the walls of the simulation box.[11] Here, we present the details of such a simulation and show that the same stratification can also be applied to account for radiation loss in Sonnet simulations of submm wave resonators. We do this by

*Address all correspondence to Akira Endo, a.endo@tudelft.nl

comparing Sonnet simulations with experiments, and a simulation using CST Microwave Studio (CST, hereafter).

For the Sonnet simulations, we have used Sonnet Version 17.56 on a Windows Server 2019 workstation with two AMD EPYC 7302 16-core processors (3 GHz), with hyper-threading (64 threads in total), and 512 GB of random access memory (16×36 GB).

2 Superconducting Submillimeter Wave Resonator

We will study the submm wave resonator shown in Fig. 1. The resonator is a meandering slotline patterned in the superconducting NbTiN ground plane on a c-plane sapphire substrate. The second harmonic mode of this resonator at 374.6 GHz is used as one of the bandpass filters in a filter bank circuit of the astronomical spectrometer Deep Spectroscopic High-redshift Mapper (DESHIMA).[14] At this frequency, the filter intercepts the submm wave signal flowing from the input port 1 to the transmission port 2 so that part of the signal is directed to the coupled port 3. The power sent to the coupled port 3 is measured with a microwave kinetic inductance detector (MKID). A previous study[14] of this resonator has shown that, at the resonance frequency, ~13% of the power from the input is radiated into the substrate. This radiative behavior makes it challenging to reproduce these results using Sonnet. Further details about the radiation mechanism of this resonator can be found in Ref. 15.

In Fig. 2, we show the model of the resonator in Sonnet. All slots in the NbTiN film are 2-μm wide. The 100-nm thick NbTiN film is modeled as a metal sheet with a surface inductance of 1 ph/sq, calculated from the resistivity (102 $\mu\Omega$ cm), critical temperature (14.7 K), and thickness (100 nm) of a NbTiN film deposited in an identical manner.[11] (The surface inductance can be calculated from the low-frequency approximation $L_s = R_s\hbar/(\pi\Delta)$, or more accurately the full Mattis–Bardeen equations, where R_s is the sheet resistance, $\hbar$ is the reduced Planck constant, and Δ is the superconducting gap energy.) The polyimide blocks under the aluminium bridges have been replaced with a vacuum layer to save computation time. The aluminium film used for the bridges is modeled as a metal sheet with a surface resistance of 0.63 $\Omega/\square$. The CPW lines have a characteristic impedance of 93 Ω. The CPW lines extend straight to the ports loaded with a matched impedance. The sapphire substrate is modeled with an anisotropic permittivity of 9.3 in the horizontal directions, and 11.9 in the vertical direction.

In the Sonnet model, all corners in the pattern are sharp, whereas the corners in the real device are rounded with a finite radius of curvature because of optical diffraction in contact mask

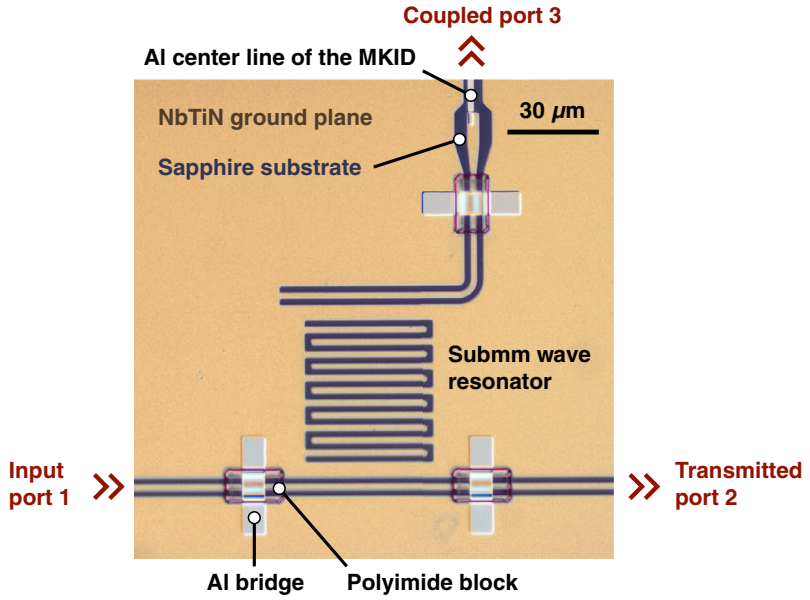

Fig. 1 Micrograph of the 374.6-GHz superconducting resonator.[14]

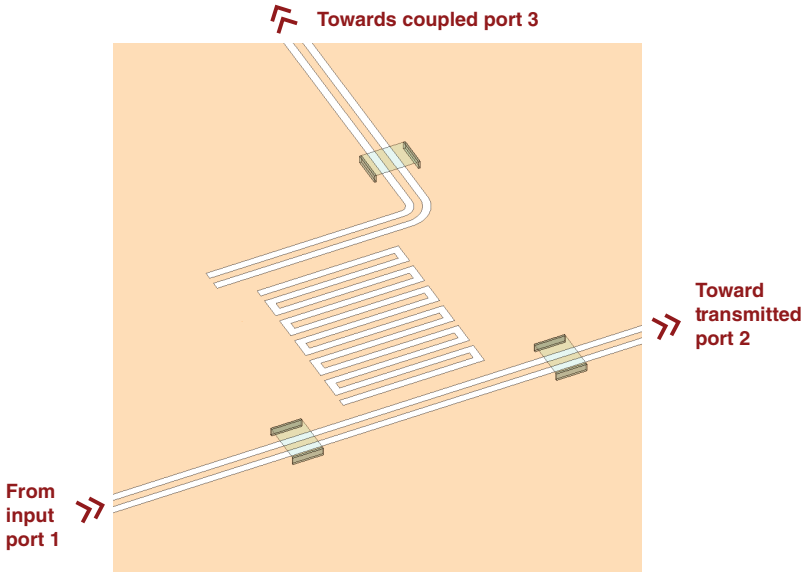

Fig. 2 Design of the submm resonator in Sonnet. The three CPW lines extend to the edge of the ground plane, where they are terminated with an impedance-matched port.

lithography. In Appendix A, we show that this difference has a negligible effect for the model presented in this article.

3 Sonnet Stratification

3.1 *Box*

Figure 3 shows the stratification of the ground plane, dielectric layers, and the box around the resonator. In Sonnet, the four sidewalls of the box must be made of PEC. The ceiling and floor are set to the free-space boundary condition. In the horizontal directions, the box is 4096 μm $\times$ 4096 μm wide. The box is much larger than the metallization, for the following reasons:

1. When the sidewalls are close to each other, the box behaves like a rectangular waveguide. This means that radiation from the structure will be restricted to the set of discrete

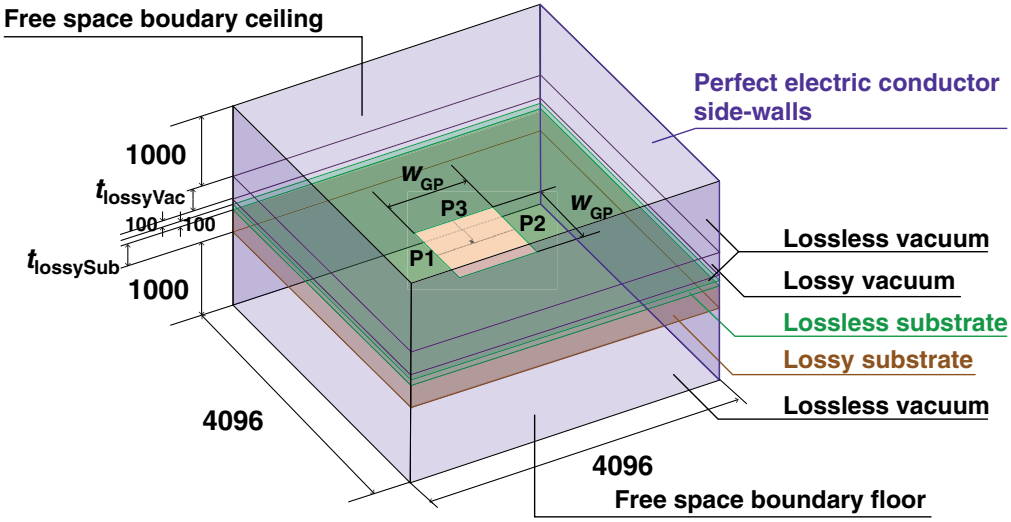

Fig. 3 Stratification for the Sonnet simulation.

waveguide modes. This can lead to suppression of radiative modes that can be excited if the structure were placed in an infinite space. The typical scale recommended in the Sonnet User's Guide is one or two times the wavelength.[7]

2. When the sidewalls are not far enough from the structure, the radiation can be reflected at the walls and couple back into the structure. To prevent this, there must be sufficient attenuation of the signal between the structure and the walls. When standing waves are observed in the current distribution, this is a strong indication that there is significant reflection.
3. The area of the ground plane is kept to the minimum, because the calculation time of Sonnet scales roughly with the number of metal subsections cubed.[10]

To model an infinite space seen by the structure, we have introduced: (1) a double-layer substrate that is designed to absorb the radiated power without affecting the waves in the resonator and CPWs. Directly under the NbTiN film layer, there is a 100-μm thick layer of sapphire with no dissipative loss. The thickness of 100 μm is much larger than the slot width of 2 μm, ensuring that all the guided waves (near field) are contained in this layer. Under this lossless substrate, there is an artificial lossy substrate that has the same anisotropic permittivity of c-plane sapphire and a loss tangent of $\tan\delta = 0.1$. (A smaller loss tangent can be used, in which case the lossy substrate must be thickened to achieve the same attenuation.) The small difference in complex permittivity between the lossless and lossy layers ensures that there is little reflection at the interface. The thickness of the lossy substrate, t_{lossy}, will be chosen so that the signal radiated from the circuit is strongly attenuated and is not reflected back to the structure. For the same reason, we have also placed an artificial layer of lossy vacuum at 100 μm above the ground plane layer to absorb radiation that is launched above the substrate, depending on the circuit that is modeled. As shown in Sec. 4.5, this layer has no effect for the cases simulated in this paper. Finally, above the lossy vacuum layer and below the lossy substrate, there are 1-mm thick layers of lossless vacuum that separate the lossy layers from the free-space boundaries at the top and bottom of the box. In the experiment, the surface of the lid was covered by carbon-loaded epoxy loaded with SiC grains. The distance from the chip to this surface was $\sim$10 mm.

3.2 *Ports*

Here, we use "co-calibrated internal ports," because this type of port can be placed on the edge of a metal that is not attached to the Sonnet box. (The most commonly used box-wall port must be attached to the box wall.) The co-calibrated internal ports are de-embedded, so the results are accurate.[7] For our simulations, we apply a floating ground node connection, which internally creates a generalized local ground (GLG) metal connection at every port.[7] This GLG metal is removed in the de-embedding process. The short calibration length of 6 μm follows from a private discussion with Sonnet, but it is not studied in detail by us.

4 Results

4.1 *'Reference' Geometry*

We will first discuss the reference geometry, of which the parameters are given in Table 1. The reference geometry is chosen as a good compromise between accuracy and calculation time. The resonator is placed close to the center of the ground plane, which is 1024-μm wide in both x and y directions. As mentioned earlier, for the NbTiN film in Sonnet, we took a sheet inductance of 1 ph/sq that is derived from measured film properties. However, we adjust the sheet inductance in CST to 0.73 ph/sq to get the resonance frequency close to the measurement. The exact reason for the different sheet inductance required in CST is not clear at the time of publication. Furthermore, to align the simulated resonance frequency to the measurement, we multiplied the Sonnet frequency by a factor of 1.0067, and the CST frequency by a factor of 0.9986.

The S-parameters calculated with Sonnet are compared with CST and measurements in Fig. 4. Because we can only use the MKID at port 3 to measure the power and we do not have

Table 1 Parameters defining the reference geometry. t_{lossySub} and t_{lossyVac} are the thicknesses of the artificial lossy layers in vacuum and below the substrate, respectively (see Fig. 3). $\tan\delta$ is the loss tangent of those layers. w_{GP} is the width of the ground plane (see Fig. 3). Δ_x and Δ_y are the offsets of the resonator position, see Fig. 6. Box size is the lateral dimension of the box (see Fig. 3).

t_{lossySub}	10^2 μm
t_{lossyVac}	10^2 μm
$\tan\delta$	10^{-1}
w_{GP}	1024 μm
Δ_x	0
Δ_y	0
Box size	4096 μm $\times$ 4096 μm

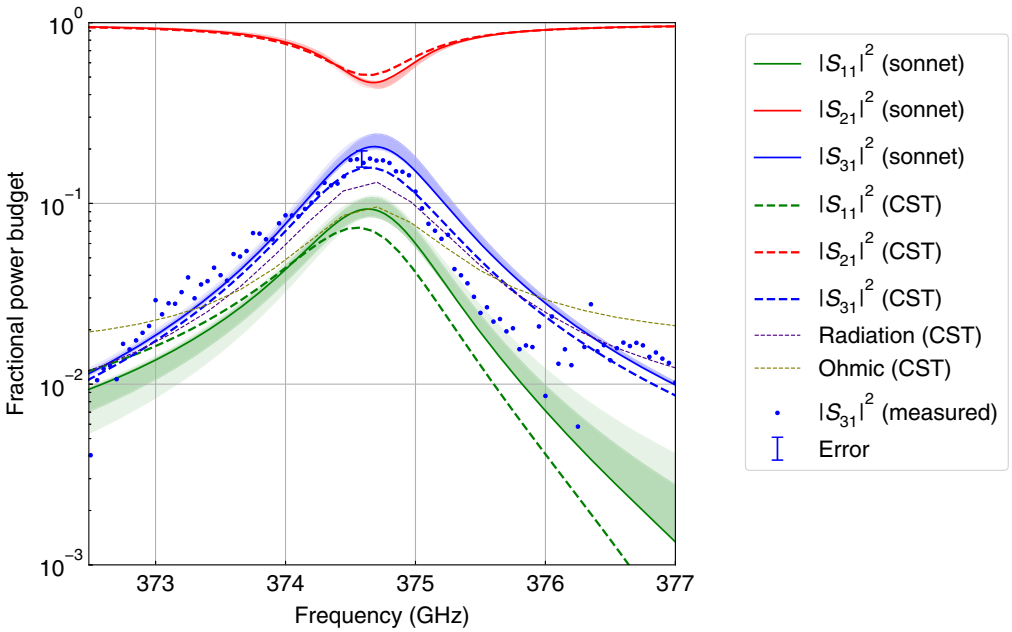

Fig. 4 Fractional power budget as a function of frequency calculated by Sonnet (solid curves) using the reference geometry, compared to the result of CST (dashed curves) and measurement[14] (points). Shaded regions that indicate the maximum–minimum range of $|S_{n1}|^2$ curves calculated with position offsets shown in Fig. 6 and Table 2. The thicker shading indicates the central 3×3 locations, and the thinner shading indicates all 5×5 locations.

any means to measure the transmitted power to port 2 and the reflected power to port 1, we can obtain only $|S_{31}|^2$ from the measurements. Therefore, we take $|S_{31}|^2$ as the prime indicator for the accuracy of the simulations. Both $|S_{31}|^2$ curves of Sonnet and CST are within the 1σ error range of the measurement[14] at the resonance peak.

The time-evolution of the current is a good indication of the presence of standing waves in the simulation box. Figure 5 is a snapshot of an animation (Video 1). The radiation leaving the resonator is not returning to the CPW, and there are no obvious indications of standing waves. (Typically, standing waves are visible if the box is too small, there is not enough dissipation in the box, etc.)

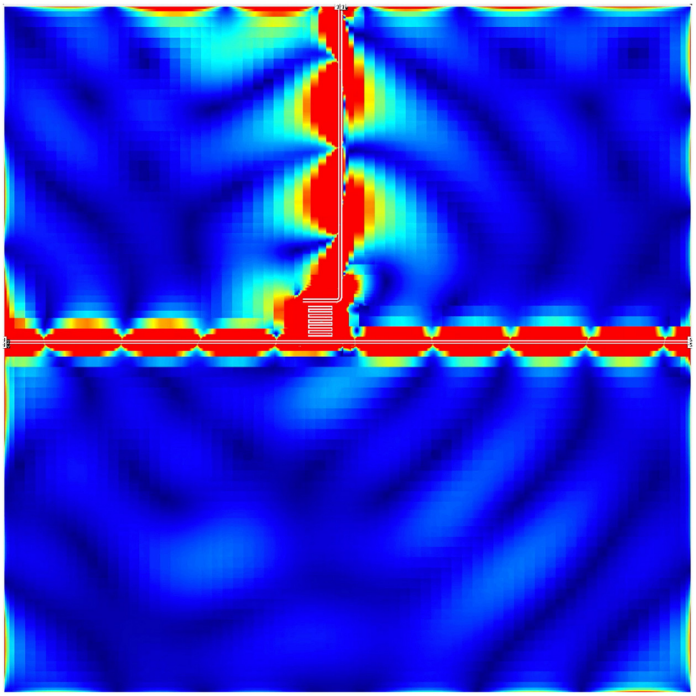

Fig. 5 Snapshot of the current distribution J_{xy} for the reference geometry. It is worth noting that the current densities plotted do not represent de-embedded data, and therefore areas near any port include the effect of the port discontinuity, according to the manual of Sonnet (Video 1, .mov, 29.7 MB [URL: https://doi.org/10.1117/1.JATIS.8.3.036005.s1]).[16]

4.2 *Sensitivity to Offsets of the Resonator Within the Ground Plane*

In Fig. 4, we show the effect of shifting the position of the resonator within the ground plane as shown in Fig. 6 and Table 2. When we take the peak value of $|S_{31}|^2$, the ratio between maximum and minimum of all positions is 1.24 (0.93 dB), which is in many cases an acceptable error tolerance for designing on-chip filters.

Interestingly, the reference position located near the center of the ground plane (hence also the center of the simulation box) yields a peak $|S_{31}|^2$ that is the lowest among all positions. This could be an indication that there remains an effect of a finite distance to the box wall or the ground plane edge. Further investigation in the directions of:

1. moving the ground plane together with the resonator inside the box and comparing the effect, and
2. repeating the simulation with larger box sizes and larger ground plane sizes

are recommended if one would want to further improve the simulation accuracy.

4.3 *Sensitivity to the Ground Plane Width*

The size of the ground plane can, in general, affect the amount of radiation loss. Here we keep the square shape of the ground plane and vary the length of the sides w_{GP} from 512 to 2048 μm, as summarized in Table 3. The result is shown in Fig. 7. Compared to the reference geometry ($w_{GP} = 1024$ μm), all other values for w_{GP} yield a slightly higher peak $|S_{31}|^2$ value. In general, we expect that the larger the ground plane the more accurate the results are, because we are trying to simulate an infinite ground plane case. However, it should be noted that the experiment was also not with an infinite ground plane; there were neighboring filter channels on both sides of the filter at a distance of $3\lambda/4$. The $|S_{31}|^2$ peak of the smallest, and hence, least accurate $w_{GP} = 512$ μm geometry has a $|S_{31}|^2$ peak that is 22% higher than the reference. The $|S_{31}|^2$ peak of the largest, $w_{GP} = 2048$ μm geometry has a $|S_{31}|^2$ peak that is 13% higher than the reference.

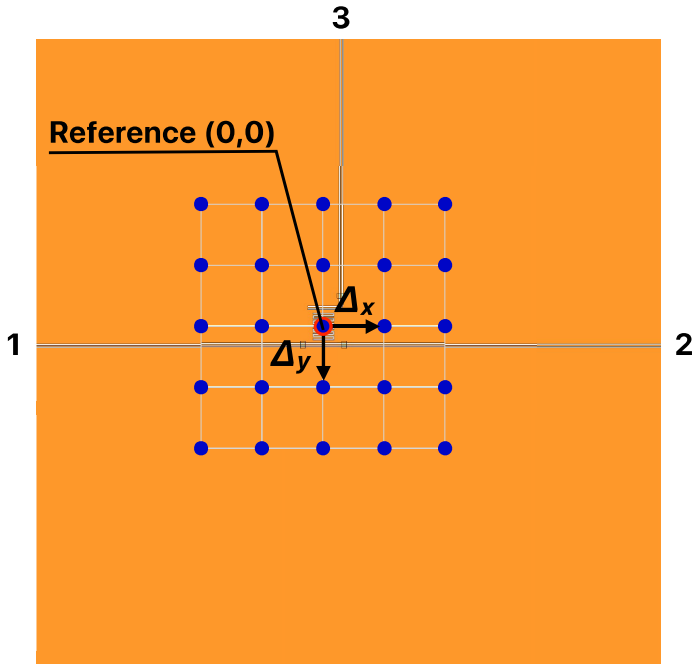

Fig. 6 Locations of the *reference* and offset positions on the 1024 μm $\times$ 1024 μm ground plane. The numbers 1–3 indicate the location of the ports.

Table 2 Parameters defining the set of geometries used to test the sensitivity to offsets of the resonator within the ground plane. Bold characters indicate the reference geometry.

t_{lossySub}	10^2 μm
t_{lossyVac}	10^2 μm
tan δ	10^{-1}
w_{GP}	1024 μm
Δ_x	-200, -100, **0**, $+100$, $+200$ μm
Δ_y	-200, -100, **0**, $+100$, $+200$ μm
Box size	4096 μm $\times$ 4096 μm

Table 3 Parameters defining the set of geometries used to test the sensitivity to the ground plane width. Bold characters indicate the reference geometry.

t_{lossySub}	10^2 μm
t_{lossyVac}	10^2 μm
tan δ	10^{-1}
w_{GP}	512, **1024**, 1536, 2048 μm
Δ_x	0
Δ_y	0
Box size	4096 μm $\times$ 4096 μm

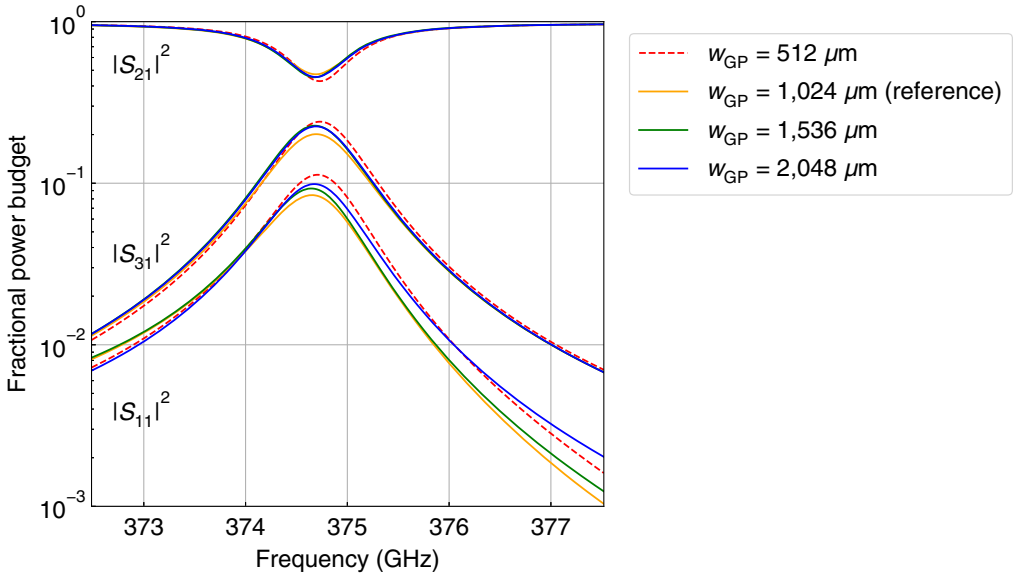

Fig. 7 The effect of changing the ground plane width, w_{GP}.

Table 4 Parameters defining the set of geometries used to test the sensitivity to the thickness of the lossy substrate. Bold characters indicate the reference geometry.

$t_{lossySub}$	0, 10^0, 10^1, **10^2**, 10^3, 10^4 μm
$t_{lossyVac}$	10^2 μm
tan δ	10^{-1}
w_{GP}	1024 μm
Δ_x	0
Δ_y	0
Box size	4096 μm × 4096 μm

4.4 *Sensitivity to the Thickness of the Lossy Substrate*

The thickness of the artificially introduced lossy substrate, $t_{lossySub}$, has been varied from 0 to 10^4 μm, as summarized in Table 4. For the 0 and 1 μm cases, the adaptive band synthesis of Sonnet had difficulties in converging after simulating at many frequencies, so eventually the simulation had to be terminated. This is most likely because there was a strong standing wave excited in the box because there was not enough attenuation under the ground plane. This shows the necessity to include this lossy layer, and we will focus on the results of $t_{lossy} = 10^1 - 10^4$ μm. Figure 8 shows the resonance peak for the different lossy-substrate thicknesses. Except for the case where the lossy substrate is the thinnest, $t_{lossySub} = 10^1$ μm, the results are completely insensitive to varying $t_{lossySub}$. This is an additional, strong indication that the waves radiated from the vicinity of the resonator are strongly attenuated by the lossy layer, thereby not returning to the circuit and not creating standing waves that affect the results.

Although large values of $t_{lossySub}$ hardly affect the simulation time, we have chosen a minimal value of $t_{lossySub} = 10^2$ μm as the reference value because it is sufficient.

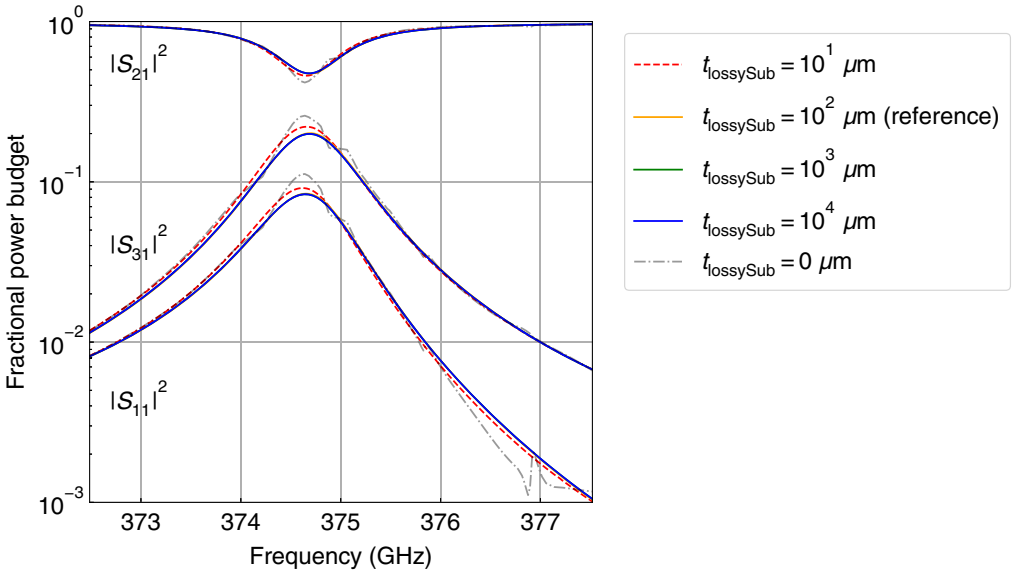

Fig. 8 Effect of changing the thickness of the lossy substrate, t_{lossySub}. The three curves for $t_{\text{lossySub}} = 10^2$ μm, 10^3 μm, and 10^4 μm are completely overlapping for all three *S*-parameters. The curve for $t_{\text{lossySub}} = 0$ μm shows substrate-resonance features, especially at around 375 and 377 GHz.

4.5 *Sensitivity to the Thickness of the Lossy Vacuum Layer*

In a similar way as the previous section, the thickness of the artificially introduced lossy vacuum layer t_{lossyVac} has been varied from 0 to 10^4 μm, as summarized in Table 5. The lossy vacuum layer has no noticeable effect on the results in the case of this model, as shown in Fig. 9. The lossy vacuum layer has no effect on the straight-CPW simulation in Sec. 5 either. This is as expected, because the radiation from these circuits is directed toward the substrate.[17] Moreover, even for geometries that might radiate toward the box ceiling, radiation could be efficiently absorbed by the free-space boundary because there is no reflective dielectric-vacuum interface in between. Nevertheless, we include the lossy vacuum layer in the box to confirm that there are no standing waves in the volume above the substrate, by an analysis as shown in Fig. 9.

4.6 *Sensitivity to the Cell Size (Meshing)*

Finally, we check that the simulation has a sufficiently small cell size (or mesh size). The reference geometry had a cell size of 0.5 μm in both x and y directions. In Fig. 10, we compare the

Table 5 Parameters defining the set of geometries used to test the sensitivity to the thickness of the lossy vacuum layer. Bold characters indicate the reference geometry.

t_{lossySub}	10^2 μm
t_{lossyVac}	0, 10^1, **10^2**, 10^3, 10^4 μm
tan δ	10^{-1}
w_{GP}	1024 μm
Δ_x	0
Δ_y	0
Box size	4096 μm × 4096 μm

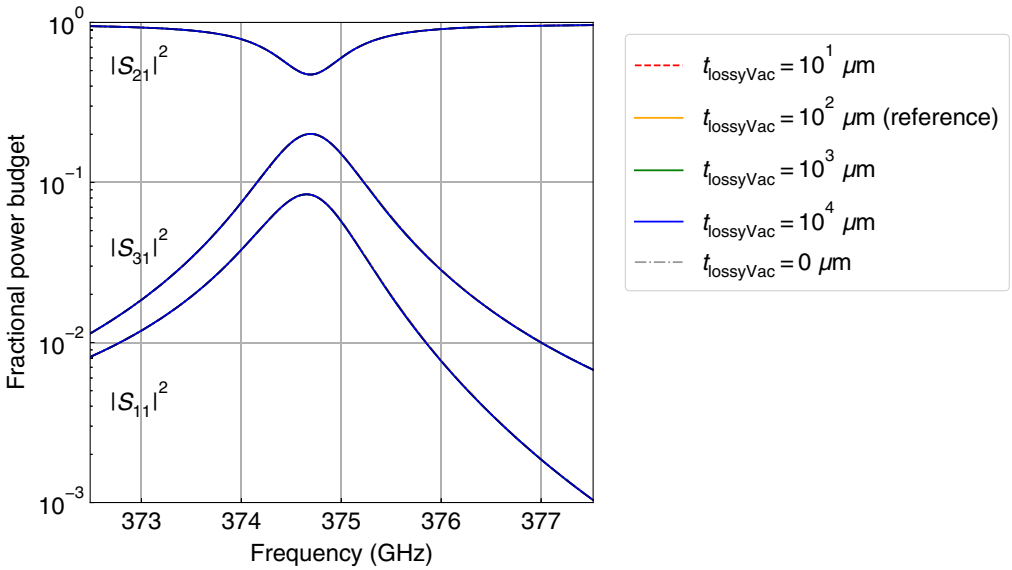

Fig. 9 Effect of changing the thickness of the lossy vacuum layer, $t_{lossyVac}$. The three curves for $t_{lossyVac} = 10^2$ μm, 10^3 μm, and 10^4 μm are completely overlapping for all three *S*-parameters.

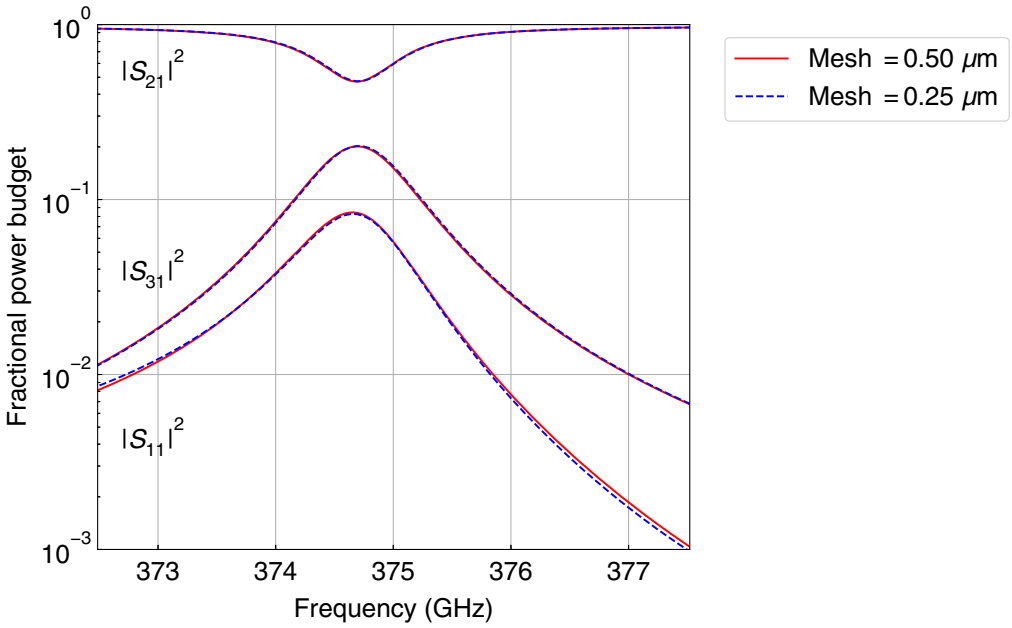

Fig. 10 Effect of changing the mesh size, from the reference value of 0.5 μm (solid curves) to 0.25 μm (dashed curves) in both *x* and *y* directions.

reference result with a simulation in which the cell size was reduced to 0.25 μm. Making the cell size smaller shifted the resonance frequency downward by a factor of 1.0096. In Fig. 10, we have multiplied the frequency of the 0.25 μm result with this factor so that the resonance frequencies match. After this correction, the two sets of curves are nearly overlapping. This result verifies that the reference geometry is sufficiently meshed.

5 Simulation of Radiation Loss from a Straight CPW

To show the general applicability of the stratification, we present the simulation of radiation loss from a straight CPW using the same stratification as the one used for the resonator. A similar

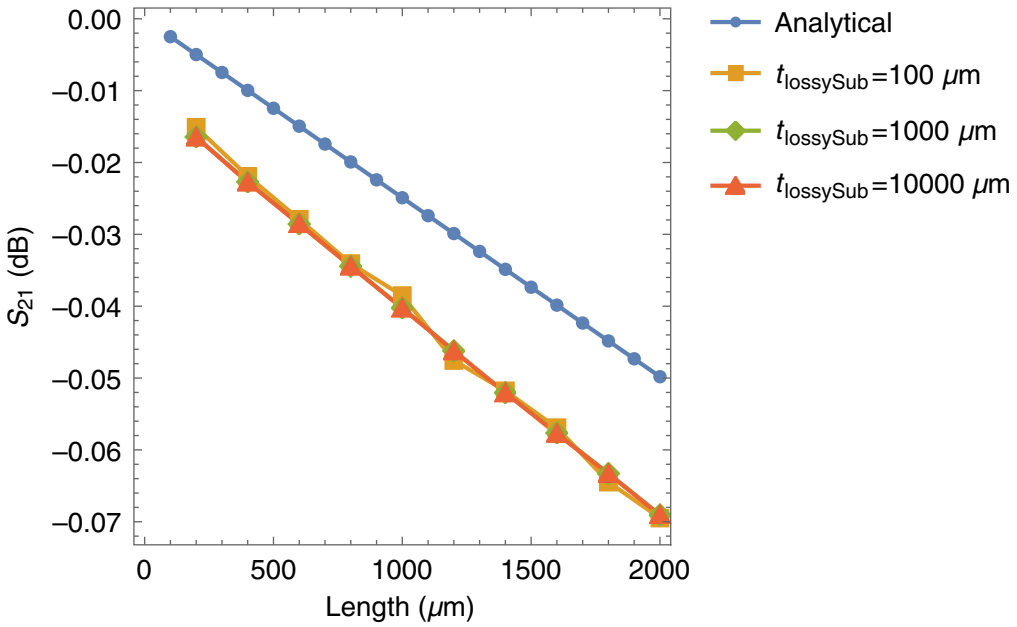

Fig. 11 Radiative loss along the $s = w = 2$ μm CPW as a function of length. The analytical line is calculated using Eq. (1). The other curves are calculated using Sonnet, for different thicknesses of the lossy dielectric, t_{lossySub}.

simulation has been presented in Ref. 11. Here, we we will compare the results to the analytical formula of Ref. 18.

We have used Sonnet to simulate the radiation loss of a straight CPW made of PEC with a center strip width of 2 μm and a slot width of 2 μm, on a silicon substrate with a relative dielectric constant of 11.44. The lateral dimensions of the Sonnet box were 3000 μm × 3000 μm. The thicknesses of the layers were the same as those of the reference geometry, except for the thickness of the lossy substrate that was varied: $t_{\text{lossySub}} = 10^2, 10^3, 10^4$ μm. Figure 11 shows the Sonnet-simulated $|S_{21}|^2$ for different CPW lengths.[11] $|S_{11}|^2$ was less than −45 dB with no clear frequency-dependence, which proves that the ports are matched well to the CPW line and reflections are negligible for this analysis. From the slope of a linear-fit to the $|S_{21}|^2$ as a function of frequency, we obtain a loss of 0.030 dB mm^{-1}. This is close to the loss of 0.025 dB mm^{-1} obtained from analytical formula of Frankel et al.[18] as follows:

$$\alpha_{\text{rad}} = \left(\frac{\pi}{2}\right)^5 2\left(\frac{\sin^4\Psi}{\cos\Psi}\right)\frac{(s+2w)^2\varepsilon_r^{3/2}}{c^3K(\sqrt{1-k^2})K(k)}f^3, \tag{1}$$

where α is the attenuation constant, $\Psi = \arccos(\sqrt{\varepsilon_{\text{eff}}/\varepsilon_{\text{r}}})$ is the radiation angle[11] (see Fig. 12. 90 deg $-\Psi$ is equivalent to the Mach angle for sonic shock waves), ε_{eff} is the effective dielectric constant of the CPW mode (defined as $\varepsilon_{\text{eff}} \equiv \sqrt{c/v_{\text{p}}}$, where v_{p} is the phase velocity), ε_{r} is the relative dielectric constant of the substrate, s is the width of the center strip of the CPW, w is the width of the CPW slots, c is the velocity of light in vacuum, $k = s/(s+2w)$, f is the frequency, and K is the complete elliptical integral of the first kind. It should be noted that the simulated data has an offset from zero loss at zero distance, most likely due to port discontinuities.

The current distribution around the CPW is shown in Fig. 12 (Video 2). The current propagates away from the CPW, showing no indication of standing waves in the vertical direction. The direction of the shock waves agrees well with $\Psi = \arccos(\sqrt{\varepsilon_{\text{eff}}/\varepsilon_{\text{r}}}) = 42.5$ deg.

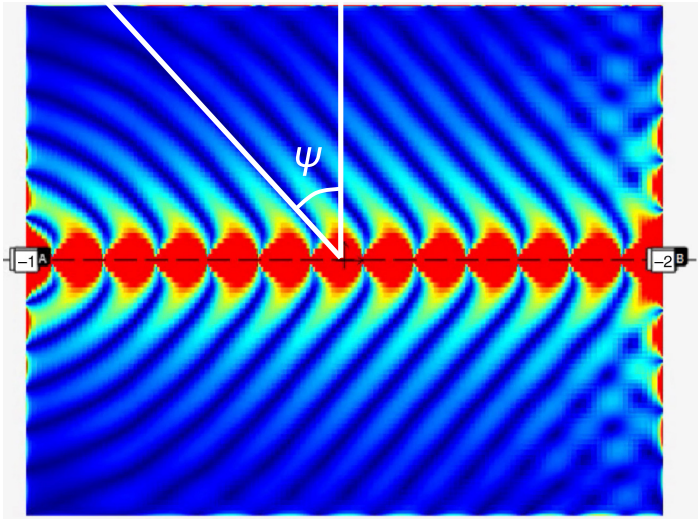

Fig. 12 Snapshot of the current distribution J_{xy} around a straight CPW. $\Psi = \arccos(\sqrt{\varepsilon_{\text{eff}}/\varepsilon_{\text{r}}}) = 42.5$ deg is derived from $\varepsilon_{\text{eff}} = 6.22$ of the CPW line calculated by Sonnet and $\varepsilon_{\text{r}} = 11.44$ of the Si substrate. Note that the current densities plotted do not represent de-embedded data, and therefore areas near any port include the effect of the port discontinuity, according to the manual of Sonnet (Video 2, .mov, 6.71 MB [URL: https://doi.org/10.1117/1.JATIS.8.3.036005.s2]).[16]

6 Discussion and Conclusion

Our results show that the 2.5-dimensional MoM solver Sonnet can be used to accurately simulate the radiation loss from planar superconducting circuits, placed in between a thick substrate and vacuum. The Sonnet simulations of the resonator reproduce the $|S_{31}|^2$ measurement result to within the error margin of the measurement. The Sonnet results are robust against variations in the geometric parameters, though it appears to be that changing the parameters studied here lead to a small systematic increase in the $|S_{31}|^2$ peak value. This could be an indication that even better accuracy could be reached by studying the effect of the box size and ground plane size, in combination, in greater detail.

7 Appendix A: Effect of Rounded Corners on the Sonnet Simulation

A potential concern when comparing the Sonnet simulation and the measurement is the resolution of lithography used to fabricate the device. We typically observe that corners that are sharp by design become rounded due to optical diffraction in ultraviolet contact-mask lithography. The radius of curvature of the corners is typically about 0.5 μm, this is also visible in the micrograph shown in Fig. 1.

Here, we have compared two Sonnet models, one with sharp corners and the other with rounded corners. We have modeled each rounded corner with three cells, as shown in Fig. 13(a). This required a mesh size of 0.25 μm. Because of this mesh size, the model with sharp corners is identical to the model with the finer mesh size investigated in Sec. 4.6.

We compare the results of rounded and sharp corners in Fig. 13. The frequencies are shifted by factors of 1.0096 and 0.99955 for the models with sharp and rounded corners, respectively, so that the peak frequencies match. It is natural that the resonance frequency is slightly different, because the rounding slightly shortens the effective electrical length of the slot. After correcting for this small frequency shift, the results are indistinguishable.

This result indicates that the rounding of corners does not have a significant effect on the conclusions in the main article about radiation loss.

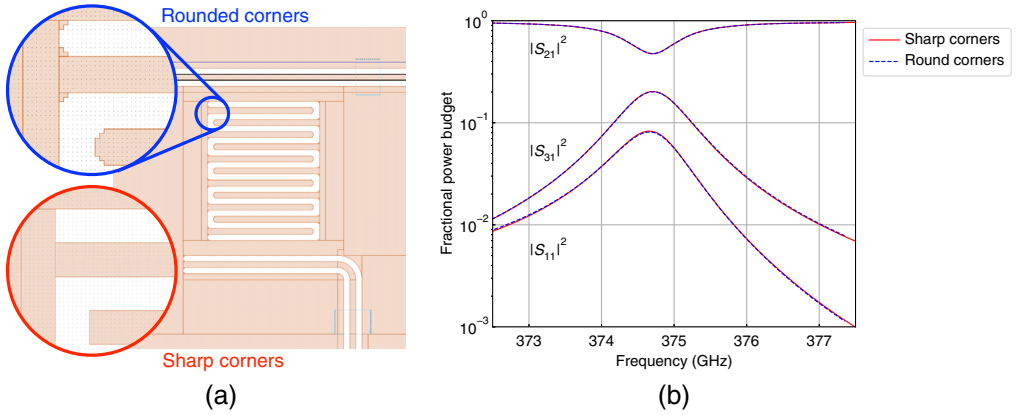

Fig. 13 (a) Geometry in Sonnet used for verifying the effect of rounding the corners of the resonator. The upper (blue) circle is a magnified view around the top left corner of the resonator with rounded corners. The lower (red) circle shows the geometry with sharp corners that is used in the main article. The grid size (visible as dots in the magnified views) is 0.25 μm. (b) Effect of rounding corners.

Acknowledgments

This paper is based on the scientific content previously reported in SPIE proceedings.[19] AE would like to thank Henry Kool and André van den Berg at ICT & Facility Management of TU Delft, for their enthusiastic support in establishing the remote-desktop server used for this research. AE would like to thank Greg Kinnetz at Sonnet for his support in setting up the Sonnet stratification. AE was supported by the Netherlands Organization for Scientific Research NWO (Vidi Grant No. 639.042.423). JJAB was the supported by the European Research Council ERC (ERC-CoG-2014—proposal No. 648135 MOSAIC).

References

1. A. Endo et al., "First light demonstration of the integrated superconducting spectrometer," *Nat. Astron.* **3**, 989–996 (2019).
2. J. van Rantwijk et al., "Multiplexed readout for 1000-pixel arrays of microwave kinetic inductance detectors," *IEEE Trans. Microwave Theory Tech.* **64**(6), 1876–1883 (2016).
3. A. Monfardini et al., "A Dual-band Millimeter-wave Kinetic Inductance Camera for the IRAM 30 m Telescope," *Astrophys. J. Suppl. Ser.* **194**, 24 (2011).
4. R. Barends et al., "Superconducting quantum circuits at the surface code threshold for fault tolerance," *Nature* **508**(7497), 500–503 (2014).
5. A. Bruno et al., "Reducing intrinsic loss in superconducting resonators by surface treatment and deep etching of silicon substrates," *Appl. Phys. Lett.* **106**(18), 182601 (2015).
6. E. F. C. Driessen et al., "Strongly disordered tin and nbtin s-wave superconductors probed by microwave electrodynamics," *Phys. Rev. Lett.* **109**, 107003 (2012).
7. "Sonnet user's guide | Sonnet," http://www.sonnetsoftware.com/support/manuals.asp
8. "CST Microwave Studio-3D EM simulation software," https://www.cst.com/products/cstmws
9. "High Frequency Structure Simulator (HFSS)," https://www.ansys.com/products/electronics/ansys-hfss
10. "How EM works | Sonnet," http://www.sonnetsoftware.com/products/sonnet-suites/how-EM-works.html
11. S. Hähnle et al., "Suppression of radiation loss in high kinetic inductance superconducting co-planar waveguides," *Appl. Phys. Lett.* **116**(18), 182601 (2020).
12. O. Noroozian et al., "Crosstalk reduction for superconducting microwave resonator arrays," *IEEE Trans. Microwave Theory Tech.* **60**, 1235–1243 (2012).
13. J. Wheeler et al., "SuperSpec, the on-chip spectrometer: improved NEP and antenna performance," *J. Low Temp. Phys.* **193**, 408–414 (2018).

14. A. Endo et al., "Wideband on-chip terahertz spectrometer based on a superconducting filterbank," *J. Astron. Telesc. Instrum. Syst.* **5**, 035004 (2019).
15. A. Pascual Laguna, "On-chip solutions for future THz imaging spectrometers," PhD thesis, Delft University of Technology (2022).
16. "Plotting conventions | Sonnet," http://www.sonnetsoftware.com/support/sonnet/help_topics/plotting_considerations.htm
17. K. J. Button, *Infrared and Millimeter Waves V10: Millimeter Components and Techniques, Part II*, Elsevier (1983).
18. M. Y. Frankel et al., "Terahertz attenuation and dispersion characteristics of coplanar transmission lines," *IEEE Trans. Microwave Theory Tech.* **39**(6), 910–916 (1991).
19. A. Endo et al., "Simulating the radiation loss of superconducting submillimeter wave filters and transmission lines using Sonnet EM," *Proc. SPIE* **11453**, 436–447 (2020).

Akira Endo is an associate professor at THz Sensing Group of TU Delft. He is interested in 3D-observations of large cosmological volumes, and the required development of (sub)millimeter-wave integral field units. He is the Dutch PI of the wideband DESHIMA spectrometer on the ASTE telescope. In 2022, he received the ERC Consolidator Grant to develop integral field units with many spaxels and to demonstrate it with astronomical observations (project TIFUUN).

Alejandro Pascual Laguna received his BSc degree in telecommunications engineering from the Universidad Pontificia Comillas, ICAI School of Engineering, Spain, in 2014, and his MSc (cum laude) and PhD degrees in electrical engineering from Delft University of Technology, The Netherlands, in 2016 and 2022 respectively. He currently works at SRON as a scientist specializing in on-chip solutions for efficient broadband sub-millimeter-wave spectrometric and imaging systems based on kinetic inductance detectors.

Sebastian Hähnle received his BSc and MSc degrees in physics from Ruprecht Karl University of Heidelberg, Germany, in 2013 and 2015, respectively, and his PhD in experimental physics from Delft University of Technology, The Netherlands, in 2021, where he worked on integrated superconducting circuits at sub-millimeter wavelengths. He currently works as a lead systems engineer at Orange Quantum Systems, developing systems for the characterization of superconducting quantum devices.

Kenichi Karatsu is an instrument scientist at SRON. He received his PhD degree in science in 2011 from Kyoto University with study of proton spin structure at the RHIC-PHENIX experiment. In 2015, he joined the DESHIMA project at TU Delft/SRON. His main role is to lead laboratory evaluation and telescope campaign of the instrument. His research interest is to develop an experimental instrument for revealing mysteries of the Universe.

David J. Thoen is working as a cleanroom engineer at TU Delft. He received his BSc degree (Hon) in applied physics from Fontys University of Applied Sciences, Eindhoven, in 2008, while he has worked as a microwave engineer at FOM Institute Rijnhuizen (now DIFFER) since 2007. Since 2010, he has worked at TU Delft on the development of microwave kinetic inductance detectors (MKID) far-infrared detectors for astronomy. He has extensive experience in cleanroom processing, process development, vacuum, and cryogenic technology.

Vignesh Murugesan is a process development engineer at SRON Netherlands Institute for Space Research. He is currently responsible for the process development and microfabrication of superconducting detectors. He received his MSc degree in microsystem integration technology from Chalmers University of Technology in 2007. He worked as a process integration engineer from 2007 to 2008 for Infineon Technologies AG. From 2010 to 2013, he worked as a MEMS process engineer for Thermo Fisher Scientific.

Jochem J.A. Baselmans is a senior instrument scientist at SRON Netherlands Institute for Space Research and full professor at THz Sensing Group of TU Delft. He leads the Dutch effort on the development of MKIDs, where his main interests are ultrasensitive devices for THz radiation detection and advanced on-chip imaging spectrometers for sub-THz imaging spectroscopy.